ARTICLE

Check for updates

Narrow-band acceleration of gold ions to GeV energies from ultra-thin foils

Philip Martin [1], Hamad Ahmed [1,2✉], Domenico Doria [1,3], Mirela Cerchez[4], Fiona Hanton[1], Deborah Gwynne[1], Aaron Alejo[1,5], Javier Fernández-Tobías[2,6], James Green[2], Andrea Macchi [7,8], David Maclellan[9], Paul McKenna [9], Jesús Álvarez Ruiz[6], Marco Swantusch[4], Oswald Willi[4], Shuhua Zhai[1,10], Marco Borghesi [1] & Satyabrata Kar [1✉]

Interaction of intense lasers with nm thick targets provides an attractive regime for the acceleration of ions of all types. Acceleration of heavy ions however is undermined in the presence of low charge contaminant species due to their higher charge-to-mass ratio. Here we show narrow-band acceleration of very heavy Au ions from ~15 nm Au foils driven by a sub-Petawatt laser, with spectral peaks of 1.5 ± 0.5 GeV at fluxes on the order of 10^{12} particles per steradian. 3D and 2D particle-in-cell simulations show a complex interplay between different acceleration mechanisms at different stages of the interaction, suggesting the spectrally peaked Au ion bunches stem from strong radiation pressure acceleration on a heavy-ion dominant plasma in the moments just before transparency, followed by an efficient acceleration due to transparency-enhanced mechanisms.

[1] Centre for Light-Matter Interactions, School of Mathematics and Physics, Queen's University Belfast, Belfast BT7 1NN, UK. [2] Central Laser Facility, Rutherford Appleton Laboratory, Didcot, Oxfordshire OX11 0QX, UK. [3] Extreme Light Infrastructure (ELI-NP), and Horia Hulubei National Institute for R&D in Physics and Nuclear Engineering (IFIN-HH), Bucharest-Magurele, Romania. [4] Institut für Laser-und Plasmaphysik, Heinrich-Heine-Universität, Düsseldorf, Germany. [5] IGFAE, Universidade de Santiago de Compostela, Santiago de Compostela, Spain. [6] Instituto de Fusion Nuclear, Universidad Politécnica de Madrid, Madrid, Spain. [7] Istituto Nazionale di Ottica, Consiglio Nazionale delle Ricerche (CNR/INO), Laboratorio Adriano Gozzini, Pisa, Italy. [8] Dipartimento di Fisica Enrico Fermi, Universitá di Pisa, Pisa, Italy. [9] Department of Physics, SUPA, University of Strathclyde, Glasgow, UK. [10] Department of Mathematics and Physics, Shanghai Normal University, Shanghai, China. ✉email: hamad.ahmed@stfc.ac.uk; s.kar@qub.ac.uk

The laser-driven acceleration of heavy ions has been of significant interest in recent years[1–4] due to its diverse range of potential applications. In particular, the acceleration of very heavy ions, such as Fe, Ag, and Au, to GeV energies and in high particle numbers has caught the attention of nuclear physics research, in the context of, for example, the fission-fusion reaction mechanism[5], which has been proposed to produce neutron-rich nuclei in the range of the astrophysical r-process. The fission-fusion mechanism demands kinetic energies of several MeV/nucleon (for instance, ca. 7 MeV/nucleon was estimated for heavy fissile ions such as ^{232}Th[5]) and very high fluxes to be efficient. Ultra-short, high flux beams of heavy ions have also been of interest over the past two decades in light of their potential use in high energy density physics[6–8], heavy ion-driven inertial fusion research[9–11], and also for injection into a conventional radiofrequency (RF) accelerator, as generation of high energy, high flux heavy ion beams has proven difficult with RF technology[12,13]. While the use of a laser driver offers the only possible route to deliver these ultra-short, spectrally bunched sources of ions, significant progress has been made with high power lasers accelerating heavy ions to multi-MeV/nucleon, albeit, so far, with a broadband, thermal spectrum that limits the number of particles at the high energy end of the spectrum[3,4,12–18].

Among a number of ion acceleration mechanisms, radiation pressure acceleration (RPA)[1,2,19–21] has drawn significant attention due to its predicted fast scaling in terms of ion energy and high laser-ion coupling efficiency. However, efficient acceleration from this mechanism has been demonstrated only for low-Z ions, such as protons and carbons[21–28], due to their favourable charge-mass ratio. These ions are usually present even in metallic targets in the form of thin surface layers of hydrocarbon contaminants. Higher-Z (i.e. lower charge-mass ratio) target species in this regime are prevented from being efficiently accelerated by these low-Z ions shielding the leading edge of the accelerating field set up by the laser's radiation pressure. The heavier ions thereafter undergo decompression and Coulomb explosion, leading to broad thermal spectra, while the lighter species are stabilized by the excess electrons released by the heavier species[21,29]. Furthermore, recent experimental results have provided evidence of early onset of relativistic transparency in ultra-thin targets (tens of nm range) irradiated at currently available laser intensities[3,29–33]. This leads to a multi-species hybrid acceleration scenario, where multiple acceleration processes (e.g. RPA, target normal sheath acceleration (TNSA), and relativistically induced transparency (RIT) enhanced acceleration) all contribute to accelerating the ions. In the case of picosecond-duration, linearly polarised pulses, the hybrid acceleration scenario becomes prevalent and unavoidable, albeit it has been shown to be favourable for the acceleration of protons[30], again, due to their favourable charge-mass ratio as compared to higher-Z bulk species. Therefore, it is extremely challenging to accelerate heavy ions with high energies and fluxes, despite several innovative approaches being used by various groups, such as cleaning contaminants by ohmic heating[34,35], or laser heating[13,14,18]; using heavy ion dopants[12,16]; and specialised double layer targetries employing carbon nanotube foams[4].

In this paper, we discuss results obtained employing ultra-thin Au foils, where, in addition to efficient acceleration of the contaminants, very significant acceleration of the heavy bulk species is observed, in spectral peaks of narrow bandwidth. Gold ions were accelerated to energies up to 2 GeV, with pronounced spectral peaks spanning the 1–2 GeV (5–10 MeV/n) range by irradiating ~ 15 nm gold foils with sub-petawatt laser pulses—to our knowledge this is the first instance of spectrally bunched acceleration of very heavy ions. Gold ions with maximum energies of ca.

5–7 MeV/n have been reported experimentally[4,13,18], and in 2D particle-in-cell (PIC) simulations[17,36], however these were in a broad exponential spectrum (attributed to a sheath acceleration dominated interaction), with a particle flux at the cut-off energy several orders of magnitude lower than what is shown here. Extensive particle-in-cell simulations indicate that a hybrid acceleration process takes place in stages, where RPA leads to the spectral bunching of Au ions only in the moments close to the onset of transparency, acting efficiently on a plasma populated predominantly by the heavy ions, followed by an efficient acceleration of the Au ion bunch in the transparency regime.

Results

Experimental results. Figure 1a shows a schematic of the experimental setup at Vulcan, the details of which can be found in the Methods section. Figure 1e, f, g shows the Au ion spectra obtained using Thomson parabola spectrometers (TPS) directed along three observation lines, from the interaction with a 15 nm (black) and a 30 nm (red) thick Au target. The Au traces for similar charge states (typically between 36–55+ for the 15 nm target, and 44–58+ for the 30 nm target) had an unavoidable overlap at energies above a few MeV/n, as can be seen in the traces shown in Fig. 1b–d. The gold ion spectra in Fig. 1e–g represent a range of charge states as labelled. The ion traces for both thicknesses were analysed by integrating the entirety of the ion signal (solid lines), and additionally, for the 15 nm target, a second charge range was analysed by selecting the signal within a range of 45–51+. Ion energies were calculated assuming an average central charge of 44+ for the 15 nm targets full signal, and 51+ for both the 30 nm targets full signal, and 15 nm targets smaller signal range. The observed charge state distribution agrees with field ionisation models for the laser intensity in our case. Higher charge states of Au ions have been recently produced, either due to higher laser intensity on target[4], or due to a strong contribution from collisional ionisation with thicker targets[18,37], which produced these high charge states only for the lowest energy Au ions, while the high energy regions of the spectrum were dominated by ionisation states best explained by the field ionisation model alone.

In contrast to the broad spectra obtained from the 30 nm targets, one can clearly observe narrow-band spectral peaks of Au ions from the 15 nm thick targets. The spectral peaks are located at the high energy end of their spectra, peaking on TPS1 at $\sim 8^{+4}_{-2}$ MeV/n. Errors in energy in this instance result from the range of overlapping charge states at high energies, as labelled in the legend in Fig. 1. Using this spectrum, the Au ion bunch across the full charge range (spanning 5–10 MeV/n) is calculated to have a flux of $\sim 8 \times 10^{11}$ particles per steradian[38]—many orders of magnitude higher than the fluxes of GeV Au ions previously reported[4,13,18]. The narrow-band spectral peaks are observed predominantly along target-normal (laser-axis) directions (TPS1 and TPS2). In the TPS spectra collected at the widest observation angle (Fig. 1g, 10°), the prominent gold spectral bunch has faded out both in terms of flux and prominence, with a significant drop in cut-off energy. This indicates that the spectrally bunched gold ion beam is produced with a small angular divergence, with a half-cone angle of ~ 10–15°.

As expected from ultra-thin targets with hydrocarbon contaminant layers, protons and carbon ions with prominent spectral peaks were observed both for the 15 nm and 30 nm targets (see Fig. 2a–c), with the peaked spectral features attributed to the influence of RPA[21]. C^{6+} spectral peaks were observed at ~ 13 MeV/n with the 15 nm targets, which represents a factor of 2 increase in energy compared to previous work[21] at similar irradiance. However, this increase in ion energy is significantly
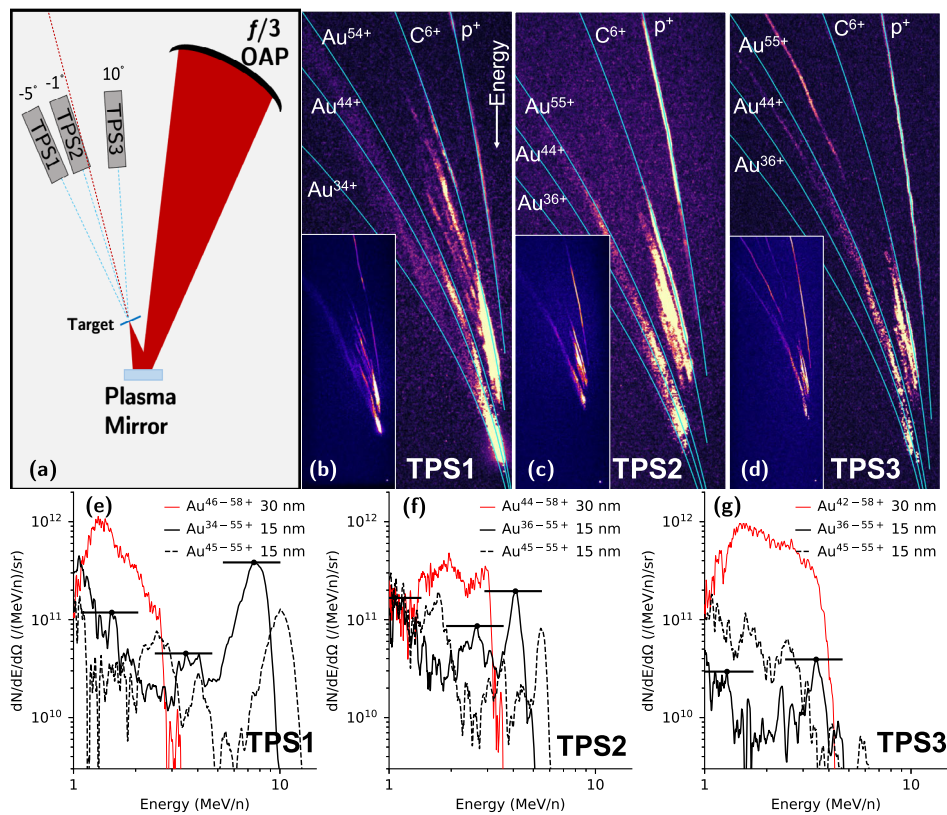
Fig. 1 Experimental setup and Au spectra. a Schematic of the experimental setup, TPS1–3 represent the three high resolution Thomson parabola spectrometers (TPS) deployed at different angles (as labelled) with respect to target normal (red dashed line). OAP (off-axis parabola) is the focusing optic. **b–d** Shows raw image plate data from each TPS on 15 nm gold foil with the highest Au ion energies obtained during the campaign. A selection of ion traces are drawn in cyan, where ion energies increase going from top to bottom on each image. Au ion traces (as labelled) represent the bounds of the charge ranges over which spectra were integrated. The insets show the full IP image. **e–g** Au ion spectra, in order from TPS1 to TPS3, for 15 nm (black) and 30 nm (red) targets. For both thicknesses, spectra are shown representing signal integration over the entirety of the charge states observed (solid lines, charge ranges are as labelled in the legend), and energies calculated assuming a central charge of $44+$ and $51+$ for the 15 and 30 nm targets, respectively. Error bars representing the energy range due to the different charge states are positioned at various points along the 15 nm spectrum. Additionally, for the 15 nm target, a second spectrum was generated integrating signal only for charges above $45+$ (dashed lines), representing most of the ion signal, at a central charge of $51+$. The difference in ion energy at the spectral peak of solid and dashed black lines is due to the chosen charge states for energy calculation. The Au ion flux in the spectrum was calculated by using the absolute calibration of the detector (BAS-TR image plate) response to laser driven Au ions shown in Ref. [38].
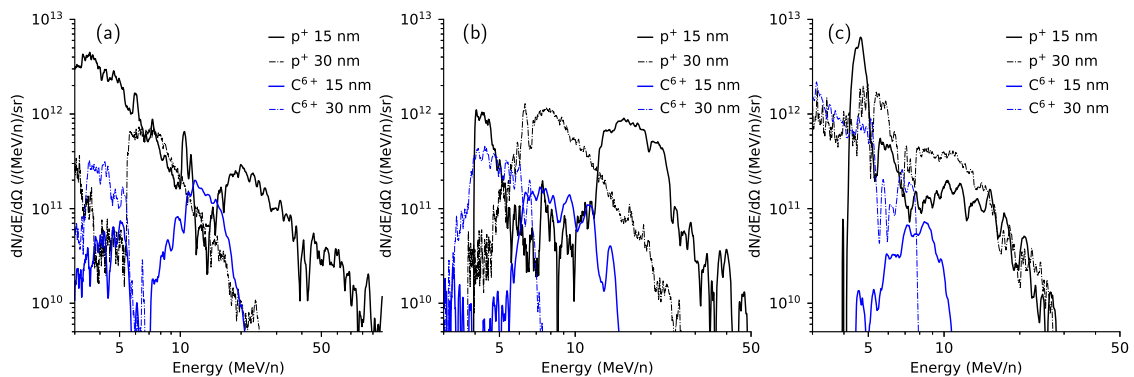

Fig. 2 Experimental proton and carbon spectra. Analysed proton (black) and C^{6+} (blue) spectra from the Thomson parabola spectrometers (TPS), for **a** TPS1, **b** TPS2, and **c** TPS3, for the same shots shown in Fig. 1. Solid lines represent the spectra for the 15 nm Au target, while dashed lines represent those from the 30 nm target.

less than what would be expected from the energy scaling in a light sail (LS) RPA dominated regime[23]. This is consistent with a premature termination of RPA, due to onset of RIT before the end of the laser pulse. A multispecies spectral bunching scenario

in a hybrid acceleration condition has been studied extensively for low-Z ion species, such as protons and carbons[19,21,25,27,31,39,40]. However, here we observe spectral bunching of the heavy bulk species, which have in previous work typically exhibited a broad,
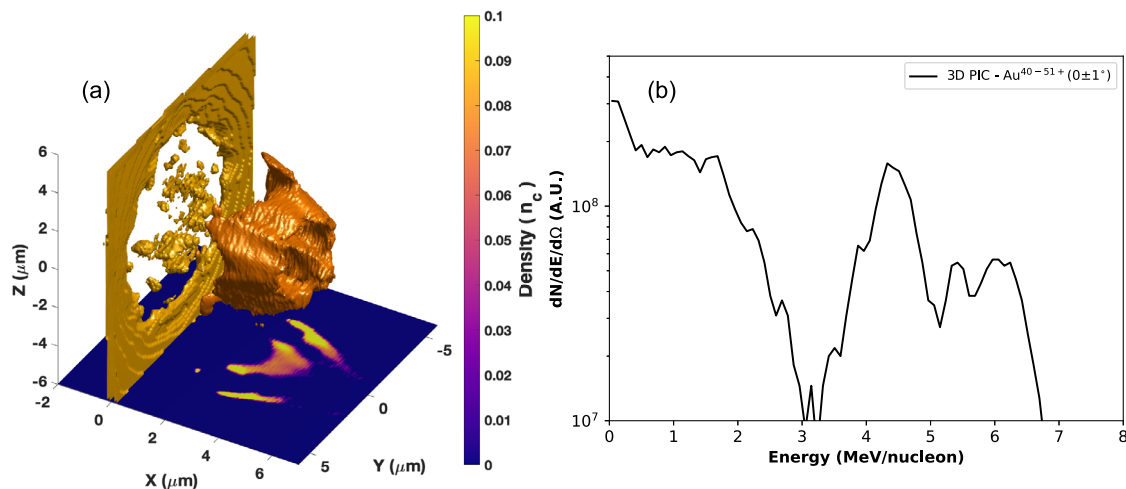
Fig. 3 3D particle-in-cell simulations showing Au ion bunch. Results of a 3D particle-in-cell (PIC) simulation showing **a** a density plot of the Au ion bunch taken at $t = +50$ fs, relative to the pulse peak, shortly after the transition to transparency. An isosurface at a density of 0.07 n_c for Au ions with energies above 0.5 MeV/n is drawn in orange. The gold region represents the high density surrounding the interaction area, showing the position of the initial unperturbed target surface. A 2D slice, through $z = 0$ μm, is also shown plotted beneath the isosurfaces, highlighting the radiation pressure acceleration-driven gold ion bunch at the centre. **b** The spectrum of Au^{40-51+} ions directed along the laser axis in a 1 degree half-cone angle, taken at $t = +600$ fs.

relatively flat spectrum[21], as is seen here for the thicker 30 nm targets (Fig. 1e–g).

Simulations. The physics underpinning the spectrally bunched acceleration of Au ions is explored via 3D and 2D particle-in-cell (PIC) simulations employing the fully relativistic code EPOCH[41]. Details on the simulation setup can be found in the Methods section. Figure 3 shows the results of the 3D simulation of a 15 nm Au target. An isosurface of Au ion density, taken at ~ 50 fs after the laser pulse peak, is plotted in Fig. 3a. A 2D slice of the data through the $z = 0$ μm plane is shown underneath the 3D plot, which highlights the distinct gold ion bunch, identifiable as the localised region of high density directed along the laser axis.

The spectrum, shown in Fig. 3(b), shows Au^{40-51+} ions, directed along the laser axis in a 1° half-angle cone, taken at ~ 600 fs after the pulse peak interaction. A spectral peak is observed at energies of ~ 4–5 MeV/n, extending to a maximum cut-off energy of ~ 7 MeV/n, similar to what was observed in the experimental data and hence highlighting the salient features of the formation of dense spectral bunch of Au ions.

To investigate the mechanism behind the bunching of gold ions in more detail, a series of 2D simulations were carried out with a higher grid resolution and larger box size. In these simulations, the intensity of the laser pulse was lowered, keeping all other initial conditions the same as in the 3D case. The 2D simulations showed the closest results to both experiment and 3D simulations for a lower intensity of ~ 10^{20}Wcm^{-2}. This is most likely due to exaggerated heating and plasma expansion in reduced dimensionality[30,42], as well as the fastest rarefaction and earlier transition to transparency in a 3D case, which in the comparison can be compensated for by implementing a lower intensity in 2D.

Figure 4 shows the results of the 2D simulations. The 15 nm target produced a gold spectral bunch, accelerated up to the high energy end of the spectrum, with bunching maintained until after the pulse. Targets thinner than 15 nm resulted in a higher maximum energy of gold ions, but with no apparent spectral peaks at the end of the simulation. Panels (a) and (b) show the time evolution of the cycle-averaged longitudinal electric field taken along a thin 0.2 μm slice centred on the laser axis. The

longitudinal positions of various electron densities are also shown in greyscale on each plot. There are distinct phases of acceleration apparent in the electric field profiles. The initial acceleration during the pulse rising edge is dominated by sheath fields, leading to an ordering of the proton, carbon, and gold ions according to charge-mass ratio, the boundaries between which can be seen in the plot as the sharp jumps in field strength, marked as 'P', and 'C', respectively. At this early stage of the interaction the laser is not intense enough for its radiation pressure to dominate the acceleration. The thermal pressure by the expanding plasma slightly overcomes the radiation pressure, forcing the critical density surface (the black line on Fig. 4a, b) backwards. As this thermal expansion causes the electron density of the target plasma to decrease over time, the influence of radiation pressure from the continuously rising pulse intensity begins to take effect. At a certain point (indicated by the dotted lines on each plot) the radiation pressure begins to dominate over the thermal pressure, resulting in the critical surface and bulk plasma ions being accelerated forward (at this point consisting mostly of low q/m ions, such as high charge state gold ions) before the onset of RIT effectively terminates RPA. The onset of transparency, corresponding to the time at which the peak density falls below the (relativistically corrected) critical density, is highlighted by the dashed lines on each plot. The relatively short RPA-dominant phase is what causes the heavy ion spectral bunching, as can be seen in the time evolution of the gold ion spectra (marked as '**B**' in Fig. 4c and d), before being post-accelerated by transparency-enhanced accelerating fields. The field ionisation model[43–46] used in the EPOCH code predicts that the Au charge state of 51+ dominates in this interaction regime due to the steep rise in ionisation potential beyond this level to the 3d subshell (Ne-like electronic configuration). As shown in Fig. 4g–h, the 51+ ionisation level is reached after the transition to transparency, where the laser pulse peak ionises the bulk plasma as it is transmitted.

Figure 4e, f show Au^{40-51+} ion spectra taken at 500 fs after the pulse peak interaction, for each target thickness. Significant Au ion spectral bunching can be seen for the 15 nm target in the on-axis direction, while for the off-axis direction, the bunching of Au ions has been less effective, showing significantly less prominent spectral peaks with lower fluxes and at lower energies, consistent
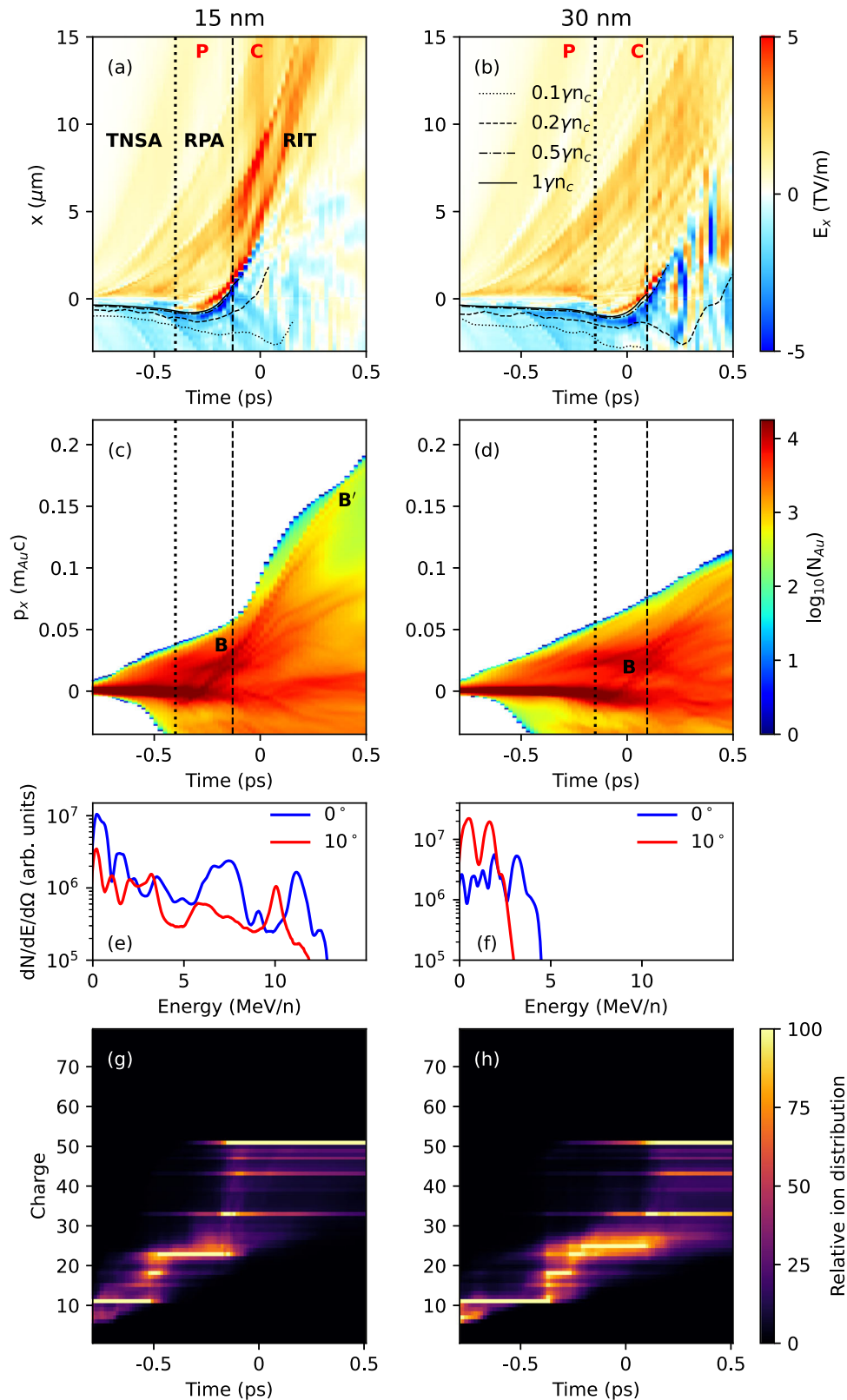
with the experimental observations. On the other hand, the 30 nm target displays ions with a spectrum devoid of significant peaked features, at a considerably lower energy, and with a more isotropic emission, as was seen in the experiment.

A semi-analytical model can be used to support the strong role of RPA for the thinnest targets. In the multi-dimensional case, the motion of the central part of the target may be described by the well-known "light sail" equation[47] with a time-varying areal density to account for the target rarefaction (note that the areal density would be constant in 1D):

$$\frac{dX}{dt} = \beta c; \quad \frac{d\beta}{dt} = \frac{2I(t - X/c)}{(\rho\ell)(t)c^2}\Gamma^{-3}R(\omega')\left(\frac{1 - \beta}{1 + \beta}\right), \quad (1)$$

where t is the time, X is the foil position, $\rho\ell(t)$ is the mass

Fig. 4 Interaction dynamics and Au spectra from simulations. 2D particle-in-cell (PIC) simulations comparing two target thicknesses, 15 nm in the first column, and 30 nm in the second. **a**, **b** Time evolution of the cycle averaged longitudinal electric field along the laser axis. The black curves indicate the positions of (relativistically corrected) electron density fronts at 0.1, 0.2, 0.5, and 1 times critical, while the vertical dotted and dashed lines indicate the transition points between each acceleration phase: target normal sheath acceleration (TNSA), Radiation pressure acceleration (RPA), and relativistically induced transparency (RIT). `P' and `C' labels represent the positions of the proton and carbon ions, which have separated according to charge-mass ratio. **c**, **d** The time evolution of the Au ion momentum spectrum (integrated over all charge states, to account for ionisation during the pulse) along the laser axis. The colorscale represents a logarithmic scale of number density of macroparticles. Time is measured relative to the incidence of the pulse peak at the initial target front surface ($x = 0$ μm). `B' and `B'' highlight the RPA-generated Au ion bunch. Au^{40-51+} ion energy spectra from the 15 nm **e** and 30 nm **f** targets are shown, taken at $t = 500$ fs, inside a 1 degree half-angle divergence directed on-axis (blue – 0°) and off-axis (red – 10°). **g, h** Temporal evolution of the charge state distribution of Au ions for both targets. The distributions are taken relative to the maximum at each time point.
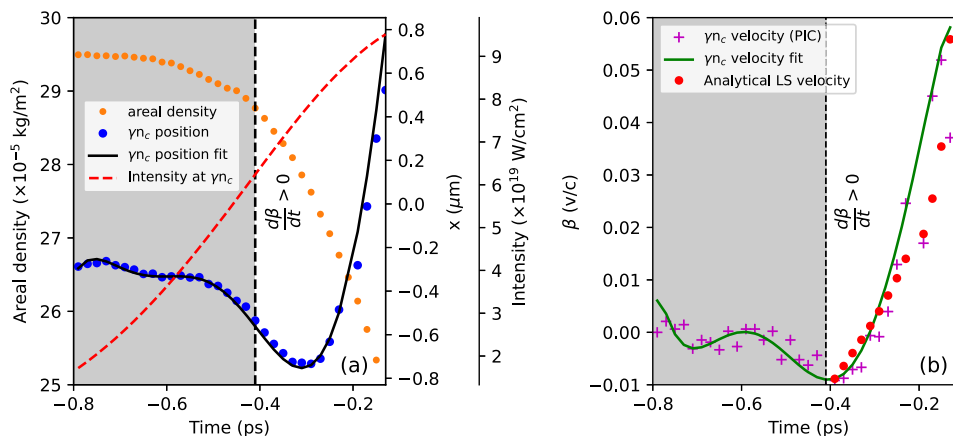

Fig. 5 Radiation pressure acceleration (RPA) dynamics in the simulation. Analysis of a 2D particle-in-cell (PIC) simulation for 15 nm Au, showing **a** the time evolution of the areal density, $\int\rho(x)dx$, of the plasma along the laser axis (orange points); the longitudinal position of the critical surface γn_c (blue points); and the intensity incident on the critical surface (red dashed line). **b** Time evolution of the critical surface velocity from the simulation (magenta crosses), plotted with the analytically derived light sail (LS) velocity from Eq. (1), taking into account the time varying areal density (red dots). Calculations were performed using a polynomial fit of the areal density and only when RPA is dominant, i.e. when acceleration is positive (the unshaded region).

density times the foil thickness, which varies in time, $I(t - X/c)$ is the incident intensity, $\beta = v/c$ is the sail velocity, $\Gamma = (1 - \beta^2)^{-1/2}$, and $R(\omega')$ is the reflectivity of the foil in its rest frame (where $\omega' = \omega\sqrt{(1 - \beta)/(1 + \beta)}$ is the laser frequency in the rest frame). Figure 5a shows how the target areal density, and the position of the critical density surface, varies in time as the laser intensity incident on the target increases. Using these points as inputs to Eq. (1), yielded a final LS velocity, for the 15 nm Au target, of $\beta \simeq 0.06$ at the point of transparency ($t \simeq -0.1$ ps), in very good agreement with the velocity extracted from the PIC simulation, as shown in Fig. 5b. This corresponds to an energy of gold ions of ~ 2 MeV/n, where the remaining energy gain is achieved, as per the simulations, during the RIT stage.

While the transparency phase can increase ion energies, depending on when RIT begins, it can also broaden, or even destroy, any quasi-monoenergetic ion spectral bunches formed during the RPA phase. In the case of the 15 nm, the RPA delivers a dense, energetic Au spectral bunch before the peak of the laser pulse, which is further accelerated efficiently by the intense laser field at the peak of the pulse. While the total ion number in the spectral bunch decreases after its initial formation, the bunch is maintained until the end of the laser pulse (marked as 'B'' in Fig. 4c), producing a spectral peak consisting primarily of Au ions with charges in the range 45–51+. Conversely, for the 30 nm target, the RPA phase is less efficient due to the increased target mass. Furthermore, the transparency-enhanced acceleration of the bunch is much less effective due to the delayed onset of RIT past the laser peak, and the laser intensity decaying rapidly with time.

Discussion

The spectrally bunched acceleration of very heavy ions such as gold from an intense laser pulse is a phenomenon that, until now, has not been observed experimentally. The phenomenon is reliant on the three stage acceleration described in this work. The first acceleration phase, dominated by sheath acceleration and plasma expansion, is necessary in order to both clear light ions away from the bulk target volume, and also to tailor the plasma areal density to an optimal point, where radiation pressure acceleration would have its greatest influence. This intra-pulse plasma tailoring cannot have as great an effect when the lasers rise time is very short, as is the case in many ultrashort pulse laser systems, which generate pulses tens of fs in duration.

We can demonstrate this by taking an example of an ultrashort laser pulse with a peak power of 10 PW (λ=0.8 μm, T$_0$=25 fs, E$_0$=250 J). These are similar parameters to multi-PW systems currently being built[48–50]. Different pulse durations were simulated, while keeping the pulse energy constant throughout. Circular polarisation was utilised in this instance for all pulses. The effect of RPA was optimised for each pulse duration by performing a thickness scan of the target and selecting the one where RIT occurred at, or close to, the pulse peak. The results of these simulations are shown in Fig. 6. It can be seen that for the relatively short pulse duration of 100 fs, the gold ions show a broad, flat spectrum. When the pulse is stretched to 150 fs and beyond, a prominent, narrow Au ion spectral bunch appears at high energy after the cut-off of the broadband, sheath-accelerated portion of the spectrum. Longer pulse durations show a similar effect, however the bunching in this scenario is less prominent.

Looking at the fraction of the total laser fluence that contributes to the RPA stage of the acceleration (Fig. 6b), defined as
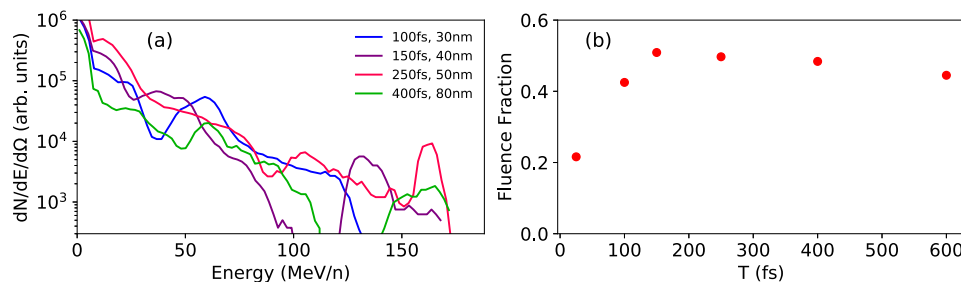
Fig. 6 Narrow-band Au acceleration with multi-petawatt lasers. a 2D particle-in-cell (PIC) simulations showing the Au spectra of the highest charge states (Au^{60-69+}) directed along (0±1)°, generated from lasers modelled on a 10 petawatt beam with circular polarisation, minimum duration 25 fs, and energy 250 J. As the pulse duration was varied, target thickness were also tailored for each duration so that RIT occurs at, or close to, the pulse peak, as defined in the legend. Intensities were calculated assuming 70% reflectivity off a plasma mirror, and 35% of the energy contained within the focal spot, 3 μm full width at half maximum (FWHM). **b** The fraction of total laser fluence that contributes to the Radiation pressure acceleration (RPA) phase plotted against pulse duration.

from when $d\beta/dt > 0$, until the onset of RIT, one can see that the gold ion bunching is optimised whenever the fraction of laser fluence contributing to RPA is maximised. From the pulse duration scans, a full width at half maximum (FWHM) duration of > 150 fs is ideal for this case. Ion energy gain tends to be exaggerated in simulations of lower dimensionality, as shown in Refs. [30,42]. As a result, the energies quoted by the 2D simulations in Fig. 6 provide only a basis to qualitatively demonstrate the physics and scalability of the mechanism. However, considering the simulated spectra in Fig. 6a, it is reasonable to predict that by tuning the laser and target parameters at multi-PW facilities, narrowband spectral bunches of very heavy ions approaching tens of GeV in energy could be obtained.

In conclusion, we have reported on the first experimental observation of narrowband beams of very heavy ions, at energies up to 2 GeV and with particle fluxes several orders of magnitude higher than what has previously been reported for laser produced heavy ions. PIC simulations suggest a complex multi-mechanism, multi-species hybrid scenario behind the formation of narrowband heavy ions, and predict that strong increases in energy can be achieved at upcoming multi-PW laser facilities. Such high-Z beams can be useful in several applications, and particularly in nuclear physics and laboratory astrophysics research.

Methods

Experimental setup. The experiment was performed using the Petawatt arm of the Vulcan laser system at the Rutherford Appleton Laboratory, United Kingdom. A schematic of the experimental setup is presented in Fig. 1a. Linearly polarised beams of central wavelength 1.054 μm were focussed on targets at near-normal incidence (measured as between 1–2°) by an f/3 off-axis parabolic mirror, after being reflected off a plasma mirror in order to improve the temporal contrast. Targets consisted of ultra-thin gold foils with thicknesses of 13 ± 5 nm and 30 ± 3 nm (referred in this manuscript as 15 nm and 30 nm targets, respectively). The ultra-thin foils were floated-off over washers which are in turn mounted on the target frames. Due to potential target deformations and tilts which can arise during deployment, the incidence angle is typically defined within an uncertainty of a few degrees. In order to avoid any potential damage to the ultra-thin targets, no attempt was made to pre-clean the target surface either by secondary laser irradiation or ohmic heating. The laser energy delivered on target was in the range (175 ± 25) J in (800 ± 100) fs duration, after considering the reflectivity of the plasma mirror (measured experimentally during the campaign). The focal spot had a Gaussian profile, with a full width at half maximum (FWHM) of ~ 5 μm, and $\sim 35\%$ of the laser energy contained within it, leading to a calculated peak intensity of

$(3 \pm 2) \times 10^{20} \mathrm{Wcm}^{-2}$. Three high resolution Thomson parabola spectrometers were deployed along observation lines looking at -5° (TPS1), -1° (TPS2), and 10° (TPS3) with respect to the laser axis, and on the same plane as the interaction. Each TPS contained a 5 cm length magnetic field of ~ 1 T, and 15 cm length E plates charged to 15–20 kV. They were each placed approximately 2 m from the interaction point, with 250 μm diameter entrance pinholes, giving rise to an acceptance solid angle on the order of 10 nsr. From these values, one can calculate the energy resolution, $\Delta E/E$, of the TPS systems to be $\sim 2\%$ for 20 MeV protons, and $\sim 8\%$ for Au^{51+} ions at energies of 1.5 GeV. The ion spectra in the TPS were recorded by Fujifilm BAS-TR image plate detectors, whose response to protons, carbon ions and gold ions were absolutely calibrated against CR-39 detectors, as described in Refs. [38,51,52].

PIC simulations. The particle-in-cell (PIC) simulations were carried out employing the fully relativistic code EPOCH[41] in 2- and 3- dimensions. In all simulations, a linearly polarised pulse with $\lambda = 1.054$ μm, a Gaussian temporal profile of 700 fs (FWHM), and a Gaussian spot of 5.6 μm (FWHM) was launched along the **x** axis. A target was placed normal to the laser direction, consisting of gold at a density of $58n_c$ (where n_c is the critical density of the laser), corresponding to a mass density of 19.3 g-/cm^3, at thicknesses of 15 nm and 30 nm, with 10 nm of hydrocarbon contaminants on both the front and rear surfaces. The contaminants contained carbon and hydrogen in the ratio CH$_2$, with densities of $20n_c$ and $40n_c$, respectively. Due to the many possible heavy ion charge states that can be present in such an interaction, dynamic ionisation was employed, using ionisation energies found on the NIST database[53]. To mitigate noise and numerical self-heating in the simulations, a current smoothing function was applied at each timestep.

For the 3D simulation shown in the manuscript for 15 nm Au target, the laser had a peak intensity of $I_0 = 2 \times 10^{20}$ W cm^{-2}. The box was 50 μm in **x**, and 20 μm in **y** and **z**, with grid resolutions of $(5 \times 25 \times 25)$ nm. The simulation was loaded with 15 particles per cell of gold, and 5 particles per cell of proton and carbon, resulting in a total particle number, after ionisation, greater than 10^9.

The 2D simulations showed the closest results to both experiment and 3D simulations for an intensity of $I_0 = 1 \times 10^{20}$ W cm^{-2}, about half the value in the 3D case. This is likely mostly due to the fastest rarefaction and earlier transition to transparency in a 3D case, as well as exaggerated longitudinal plasma expansion in 2D, particularly in the RIT regime[30,42], which in the comparison can be compensated for by a lower intensity in 2D. The simulation box in this case was 110 μm in **x**,

and 80 μm in **y** with a spatial resolution of 5 nm, and 10 nm, respectively. There were 500 particles per cell and per species, loaded initially into the simulation.

Data availability

References

1. Macchi, A., Borghesi, M. & Passoni, M. Ion acceleration by superintense laser-plasma interaction. *Rev. Mod. Phys.* **85**, 751–793 (2013).
2. Daido, H., Nishiuchi, M. & Pirozhkov, A. S. Review of laser-driven ion sources and their applications. *Rep. Prog. Phys.* **75**, 056401 (2012).
3. Palaniyappan, S. et al. Efficient quasi-monoenergetic ion beams from laser-driven relativistic plasmas. *Nat. Commun.* **6**, 10170 (2015).
4. Wang, P. et al. Super-heavy ions acceleration driven by ultrashort laser pulses at ultrahigh intensity. *Phys. Rev. X* **11**, 21049 (2021).
5. Habs, D. et al. Introducing the fission-fusion reaction process: using a laser-accelerated Th beam to produce neutron-rich nuclei towards the N=126 waiting point of the r-process. *Appl. Phys. B: Lasers Opt.* **103**, 471–484 (2011).
6. Dewald, E. et al. Fundamental studies of intense heavy-ion beam interaction with solid targets. *IEEE Trans. Plasma Sci.* **31**, 221–226 (2003).
7. Tahir, N. A., Hoffmann, D. H., Maruhn, J. A., Spiller, P. & Bock, R. Heavy-ion-beam-induced hydrodynamic effects in solid targets. *Phys. Rev. E - Stat. Phys., Plasmas, Fluids, Relat. Interdiscip. Top.* **60**, 4715–4724 (1999).
8. Tahir, N. A. et al. Application of intense heavy ion beams to study high energy density physics. *Plasma Physics and Controlled Fusion* **53** (2011).
9. Basko, M. M. New developments in the theory of ICF targets, and fast ignition with heavy ions. *Plasma Phys. Controlled Fusion* **45**, A125–A132 (2003).
10. Honrubia, J. J., Fernández, J. C., Temporal, M., Hegelich, B. M. & Meyer-ter Vehn, J. Fast ignition of inertial fusion targets by laser-driven carbon beams. *Phys. Plasma* **16**, 102701 (2009).
11. Honrubia, J., Fernández, J., Hegelich, B., Murakami, M. & Enriquez, C. Fast ignition driven by quasi-monoenergetic ions: optimal ion type and reduction of ignition energies with an ion beam array. *Laser Part. Beams* **32**, 419–427 (2014).
12. Nishiuchi, M. et al. Acceleration of highly charged GeV Fe ions from a low-Z substrate by intense femtosecond laser. *Phys. Plasmas* **22**, 1–9 (2015).
13. Lindner, F. H. et al. En-route to the fission–fusion reaction mechanism: a status update on laser-driven heavy ion acceleration. *Plasma Phys. Controlled Fusion* **61**, 055002 (2019).
14. Nishiuchi, M. et al. Dynamics of laser-driven heavy-ion acceleration clarified by ion charge states. *Phys. Rev. Res.* **2**, 33081 (2020).
15. Braenzel, J. et al. Coulomb-driven energy boost of heavy ions for laser-plasma acceleration. *Phys. Rev. Lett.* **114**, 124801 (2015).
16. Tayyab, M. et al. Mono-energetic heavy ion acceleration from laser plasma based composite nano-accelerator. *Phys. Plasma* **25**, 123102 (2018).
17. Petrov, G. M., Mcguffey, C., Thomas, A. G. R., Krushelnick, K. & Beg, F. N. Generation of heavy ion beams using femtosecond laser pulses in the target normal sheath acceleration and radiation pressure acceleration regimes. *Physics of Plasmas* **23** (2016).
18. Lindner, F. H. et al. Charge-state resolved laser acceleration of gold ions to beyond 7 MeV/u. *Sci. Rep.* **12**, 1–11 (2022).
19. Esirkepov, T., Borghesi, M., Bulanov, S. V., Mourou, G. & Tajima, T. Highly efficient relativistic-ion generation in the laser-piston regime. *Phys. Rev. Lett.* **92**, 2–5 (2004).
20. Robinson, A. P. L., Zepf, M., Kar, S., Evans, R. G. & Bellei, C. Radiation pressure acceleration of thin foils with circularly polarized laser pulses. *New J. Phys.* **10** (2008).
21. Kar, S. et al. Ion acceleration in multispecies targets driven by intense laser radiation pressure. *Phys. Rev. Lett.* **109**, 1–5 (2012).
22. Bulanov, S. V. et al. Unlimited ion acceleration by radiation pressure. *Phys. Rev. Lett.* **104**, 1–4 (2010).
23. Macchi, A., Veghini, S. & Pegoraro, F. "Light Sail" Acceleration Reexamined. *Phys. Rev. Lett.* **103**, 1–4 (2009).
24. Klimo, O., Psikal, J., Limpouch, J. & Tikhonchuk, V. T. Monoenergetic ion beams from ultrathin foils irradiated by ultrahigh-contrast circularly polarized laser pulses. *Phys. Rev. Spec. Top. Accel. Beams* **11**, 031301 (2008).
25. Steinke, S. et al. Stable laser-ion acceleration in the light sail regime. *Phys. Rev. ST Accel. Beams* **16**, 011303 (2013).
26. Yu, T.-P., Pukhov, A., Shvets, G. & Chen, M. Stable Laser-Driven Proton Beam Acceleration from a Two-Ion-Species Ultrathin Foil. *Phys. Rev. Lett.* **105**, 065002 (2010).
27. Scullion, C. et al. Polarization dependence of bulk ion acceleration from ultrathin foils irradiated by high-intensity ultrashort laser pulses. *Phys. Rev. Lett.* **119**, 054801 (2017).
28. McIlvenny, A. et al. Selective ion acceleration by intense radiation pressure. *Phys. Rev. Lett.* **127**, 194801 (2021).
29. Qiao, B. et al. Radiation-pressure acceleration of ion beams from nanofoil targets: the leaky light-sail regime. *Phys. Rev. Lett.* **105**, 8–11 (2010).
30. Higginson, A. et al. Near-100 MeV protons via a laser-driven transparency-enhanced hybrid acceleration scheme. *Nat. Commun.* **9**, 1–9 (2018).
31. Dover, N. P. et al. Buffered high charge spectrally-peaked proton beams in the relativistic-transparency regime. *New J. Phys.* **18** (2016).
32. Powell, H. W. et al. Proton acceleration enhanced by a plasma jet in expanding foils undergoing relativistic transparency. *N. J. Phys.* **17**, 103033 (2015).
33. Yin, L., Albright, B. J., Hegelich, B. M. & Fernández, J. C. Gev laser ion acceleration from ultrathin targets: the laser break-out afterburner. *Laser Part. Beams* **24**, 291–298 (2006).
34. Hegelich, B. M. et al. Laser acceleration of quasi-monoenergetic MeV ion beams. *Nature* **439**, 441–444 (2006).
35. McKenna, P. et al. Low- and medium-mass ion acceleration driven by petawatt laser plasma interactions. *Plasma Phys. Controlled Fusion* **49**, B223–B231 (2007).
36. Petrov, G. M., McGuffey, C., Thomas, A. G., Krushelnick, K. & Beg, F. N. Heavy ion acceleration in the radiation pressure acceleration and breakout afterburner regimes. *Plasma Physics and Controlled Fusion* **59** (2017).
37. Afshari, M. et al. The role of collisional ionization in heavy ion acceleration by high intensity laser pulses. *Sci. Rep.* **12**, 1–8 (2022).
38. Doria, D. et al. Calibration of BAS-TR image plate response to GeV gold ions. *Rev. Sci. Instrum.* **93**, 033304 (2022).
39. Henig, A. et al. Radiation-pressure acceleration of ion beams driven by circularly polarized laser pulses. *Phys. Rev. Lett.* **103**, 3–6 (2009).
40. Schlegel, T. et al. Relativistic laser piston model: Ponderomotive ion acceleration in dense plasmas using ultraintense laser pulses. *Physics of Plasmas* **16** (2009).
41. Arber, T. D. et al. Contemporary particle-in-cell approach to laser-plasma modelling. *Plasma Phys. Control. Fusion* **57** (2015).
42. Stark, D. J., Yin, L., Albright, B. J. & Guo, F. Effects of dimensionality on kinetic simulations of laser-ion acceleration in the transparency regime. *Physics of Plasmas* **24** (2017).
43. Popov, V. S. Tunnel and multiphoton ionization of atoms and ions in a strong laser field (Keldysh theory). *Phys. -Usp.* **47**, 855 (2004).
44. Nikishov, A. I. & Ritus, V. I. *Sov. Phys. JETP* **23** (1966).
45. Nikishov, A. I. & Ritus, V. I. *Sov. Phys. JETP* **25** (1967).
46. Perelopov, A. M., Popov, V. S. & Terent, M. V. *Sov. Phys. JETP* **23** (1966).
47. Macchi, A., Veghini, S., Liseykina, T. V. & Pegoraro, F. Radiation pressure acceleration of ultrathin foils. *N. J. Phys.* **12**, 045013 (2010).
48. https://eli-laser.eu/ (2021).
49. https://apollonlaserfacility.cnrs.fr/en/laser-beams/ (2021).
50. Gan, Z. et al. *The Shanghai Superintense Ultrafast Laser Facility (SULF) Project*, 199–217 (Springer International Publishing, Cham, 2021).
51. Martin, P. et al. Absolute calibration of Fujifilm BAS-TR image plate response to laser driven protons up to 40 MeV. *Rev. Sci. Instrum.* **93**, 053303 (2022).
52. Doria, D. et al. Calibration of BAS-TR image plate response to high energy (3–300 MeV) carbon ions. *Rev. Sci. Instrum.* **86** (2015).
53. Kramida, A., Ralchenko, Y., Reader, J. & NIST ASD Team. NIST Atomic Spectra Database (ver. 5.6.1), [Online]. Available: https://physics.nist.gov/asd. National Institute of Standards and Technology, Gaithersburg, MD. (2018).
54. Kar, S., Martin, P. & Ahmed, H. Dataset for "Narrow-band acceleration of gold ions to GeV energies from ultra-thin foils" https://doi.org/10.17034/a87b2bb1-4312-4813-b590-e608807300df (2023).

Acknowledgements

Author contributions

S.K. and M.B. conceived and managed the project. Experimental work was carried out by H.A., D.D., M.C., F.H., D.G., A.A., J.F.-T., J.G., D.M., J.A.-R., P.McK., O.W., and M.S.; Data analysis was carried out by P.M., F.H., and S.Z.; PIC simulations were carried out by P.M. with guidance from A.M.; the original draft was prepared by P.M. and S.K., and subsequent revisions performed by all authors.

Competing interests

The authors declare no competing interests.

Additional information

Supplementary information The online version contains supplementary material available at https://doi.org/10.1038/s42005-023-01425-4.

Correspondence and requests for materials should be addressed to Hamad Ahmed or Satyabrata Kar.

Peer review information *Communications Physics* thanks the anonymous reviewers for their contribution to the peer review of this work. A peer review file is available.

Reprints and permission information is available at http://www.nature.com/reprints

Publisher's note Springer Nature remains neutral with regard to jurisdictional claims in published maps and institutional affiliations.